

1
2
3
4
5
6
7
8
9
10
11
12
13
14
15
16
17
18
19
20
21

PROFESSOR NATHAN JEFFERY (Orcid ID : 0000-0001-5166-2029)

Article type : Original Paper

Corresponding author mail id: njeffery@liv.ac.uk

Ontogenetic and *in-silico* models of spatial-packing in the hypermuscular mouse skull

N. S. Jeffery¹, D. Sarver^{2,3} and C.L. Mendias^{2,4}

1. Institute of Life Course & Medical Sciences, University of Liverpool, UK
2. Department of Orthopaedic Surgery, University of Michigan, USA
3. School of Medicine, Johns Hopkins University, USA
4. HSS Research Institute, Hospital for Special Surgery, USA

This is the author manuscript accepted for publication and has undergone full peer review but has not been through the copyediting, typesetting, pagination and proofreading process, which may lead to differences between this version and the [Version of Record](#). Please cite this article as [doi: 10.1111/JOA.13393](https://doi.org/10.1111/JOA.13393)

This article is protected by copyright. All rights reserved

22
23
24
25
26
27
28
29
30
31
32
33
34
35
36
37
38
39
40
41
42
43
44
45
46
47
48
49

Author Manuscript

Keywords: spatial-packing, masseter, endocranial, myostatin, mouse

Abstract

Networks linking single genes to multiple phenotypic outcomes can be founded on local anatomical interactions as well as on systemic factors like biochemical products. Here we explore the effects of such interactions by investigating the competing spatial demands of brain and masticatory muscle growth within the hypermuscular myostatin deficient mouse model and in computational simulations. Mice that lacked both copies of the myostatin gene (-/-) and display gross hypermuscularity, and control mice that had both copies of the myostatin gene (+/+) were sampled at 1, 7, 14 and 28 postnatal days. A total of 48 mice were imaged with standard as well as contrast-enhanced microCT. Size metrics and landmark configurations were collected from the image data and were analysed alongside *in-silico* models of tissue expansion. Findings revealed that: masseter muscle volume was smaller in

50 -/- mice at 1 day but became, and remained thereafter, larger by 7 days; -/- endocranial
51 volumes begin and remained smaller; -/- enlargement of the masticatory muscles was
52 associated with caudolateral displacement of the calvarium, lateral displacement of the
53 zygomatic arches, and slight dorsal deflection of the face and basicranium. Simulations
54 revealed basicranial retroflexion (flattening) and dorsal deflection of the face associated with
55 muscle expansion and abrogative covariations of basicranial flexion and ventral facial
56 deflection associated with endocranial expansion. Our findings support the spatial-packing
57 theory and highlight the importance of understanding the harmony of competing spatial
58 demands that can shape and maintain mammalian skull architecture during ontogeny.

59
60
61
62
63
64
65
66
67
68
69
70
71
72
73
74
75
76
77

Author Manuscript

79 **Introduction**

80 Anatomical structures physically interact to varying degrees throughout ontogeny, adulthood,
81 and evolution. During ontogeny, genetically mediated changes in one structure can
82 simultaneously affect important epigenetic changes in several surrounding structures.
83 Moreover, interactions that reliably generate the same or similar phenotypes over successive
84 ontogenies can shield from selection mutations in genes that would have otherwise
85 predominantly shaped those affected structures (see Green et al., 2017; Zheng et al. 2019;
86 Lahti et al., 2009). These mutations can then accumulate, leading to punctuated phenotypic
87 diversification as conditions prevail that destabilise the protective network of interactions and
88 expose the gene variants to selection (Gould, 2002; Laland et al., 2015). Interactions also
89 allow for phenotypic adjustments during life, which can accommodate behavioural changes
90 of, for example, dietary niche or physical activity (e.g. Anderson et al., 2014). This capability
91 extends into adulthood and can help genetically similar individuals and populations to tolerate
92 and thrive under different environmental conditions (see Murren et al, 2015). The premise that
93 structural interactions help define and maintain morphological outcomes has a long history
94 and has taken many forms over the decades (e.g. Kappers, 1932; Neubauer, 1925;
95 Weidenreich, 1941; Weiss, 1933; Wolff, 1893). Most relevant to this paper are paradigms that
96 define specific, typically spatially co-ordinated networks of interactions such as the functional
97 matrix hypothesis formulated by Moss (Moss & Young, 1960) and its derivative, the spatial-
98 packing hypothesis popularised by Ross (Ross & Ravosa, 1993). More recently, the concept
99 has also become implicit to theories of morphological integration and modularity (e.g.
100 Goswami et al., 2015; Klingenberg, 2014). Here we explore the spatial-packing hypothesis.

101 The central tenet of the spatial-packing hypothesis is that the head has a finite capacity to
102 accommodate and maintain the functional integrity of a range of structures. Once spatially
103 optimised, any subsequent relative expansion of one structure necessitates changes of form
104 or function of one or more of its neighbouring structures. Lesciotto and Richtsmeier (2019)
105 offer an excellent comprehensive review of the core principles (see also Lieberman et al.,
106 2000; Singleton, 2013). Expansion of the brain is most often studied in this context, particularly
107 amongst highly encephalised primates. There is substantial empirical evidence from adult
108 interspecific studies and from the fossil record to support the notion that the primate skull,
109 particularly the basicranium and face as well as the neurocranium, changed shape to fit
110 relative expansion of the brain (e.g. Ross & Ravosa, 1993; Ross & Henneberg, 1995; Bastir
111 et al., 2010). An often-cited competing spatial demand to brain expansion is the relative size
112 of the masticatory apparatus. Biegert (1963) was first to outline this trade-off, suggesting that

113 expansion of the masticatory apparatus relative to the brain constrains brain-related changes
114 of the skull. Again, there is strong support from adult interspecific studies as well as the fossil
115 record (e.g. Ross & Ravosa, 1993; Ross & Henneberg, 1995; Veneziano et al. 2019; Neaux
116 et al., 2015). The mechanism(s) by which the skull responds to such competing spatial
117 demands during ontogeny are unclear. It seems likely that strain gradients created by
118 expanding tissues trigger cellular activity and incremental architectural remodelling (see
119 Enlow, 1962 and, for example, more recently Edamoto et al. 2019). However, whilst the
120 mechanotransduction of muscle and kinematic forces is well documented (see reviews by
121 Stewart et al., 2020; Vincent & Wann, 2019), we know comparatively little about the efficacy
122 of the low amplitude and low frequency stimuli elicited by tissue expansion. Another, congruent
123 agent could be straightforward mechanical deformation –skull features are shaped and held
124 in place by tissue growth in a way that is defined by the geometry, relative rigidity and spatial
125 relationships of the tissues involved. This is reminiscent of the analogy popularised by Enlow
126 (1976), and others, in which an inflating balloon bends around a piece of tape adhered to its
127 surface.

128

129 Here we evaluate the potential of simple mechanical deformation to describe changes of skull
130 shape and we also test Biegert's spatial-packing hypothesis using a myostatin (GDF-8) knock-
131 out mouse model of hypermuscularity. Myostatin is a member of the transforming growth
132 factor-beta (TGF- β) superfamily and acts as a negative regulator of skeletal muscle growth in
133 vertebrates. It signals via type IB and IIB activin receptors to inhibit muscle progenitor cell
134 proliferation, activate proteolytic systems, and inhibit protein synthesis in the mature muscle.
135 A loss of the gene encoding myostatin results in a greatly increased skeletal muscle mass, via
136 fiber hypertrophy and hyperplasia (Mendias et al., 2006). Previous studies have shown
137 significant increases of masseter mass among myostatin knock-out (-/-) mice in adults and at
138 a range of ontogenetic time-points (e.g. Cray et al, 2011; Vecchione et al, 2010). Volumes
139 reported by Jeffery & Mendias (2014) further confirmed masseter enlargement and revealed
140 for the first time an associated reduction of brain size.

141 We use the latest advances of contrast-enhanced microCT, non-Euclidean geometric
142 morphometrics as well as computational tissue modelling to test for shape changes that co-
143 vary with enlargement of the masticatory muscles relative to brain size during ontogeny. Our
144 spatial-packing hypothesis has two parts. The first part states that masticatory muscle
145 enlargement constrains brain growth as implied by Stedman et al (2004) (see also Anthony,
146 1903). This predicts a close association between the ontogenetic timing of hypermuscularity
147 and the reduced brain size seen in adult -/- mice. The second part follows Biegert's (1963)

148 proposal that relative masticatory muscle enlargement constrains the effects of brain growth
149 on the surrounding skull. This predicts that skull markers of brain expansion, such as base
150 flexion and klinorhynch (ventral facial deflection), are diminished among *-/-* mice. However,
151 in our *-/-* mouse model the spatial-packing problem of enlarged musculature is conflated with
152 reduced brain size, possibly due to suppressed myostatin expression within the brain (see
153 Discussion), and with the structural effects of increased muscle and bite force (e.g. Byron et
154 al., 2006; Williams et al, 2015). We therefore inferred the extricated and combined effects of
155 brain and muscle growth on skull architecture *in-silico* and in doing so we also evaluate the
156 ability of simple deformation to describe spatial-packing related phenomena. Simulations were
157 evaluated empirically with reference to previously published observations notionally linked to
158 spatial-packing. Predictions included: basicranial flexion and ventral facial deflection
159 associated with simulated brain expansion (e.g. e.g. Ross & Ravosa, 1993); basicranial
160 flattening and dorsal facial deflection (airorhynch) associated with simulated muscle
161 expansion (e.g. Ross & Henneberg, 1995); diminished basicranial flexion and diminished
162 ventral facial deflection associated with simulated brain and muscle expansion (e.g. Biegert,
163 1963).

164

165 **Methods**

166 *Sample:* Control (+/+) and myostatin deficient (-/-) mice on a C57BL/6J background were
167 reared and culled at the University of Michigan in strict accordance with Institutional Animal
168 Care & Use Committee approval (PRO6079). Mice share a common maternal genotype and
169 both sets of parents and offspring were reared under standardised laboratory conditions. A
170 total of 48 male mice were sampled at 1, 7, 14 & 28 postnatal days (6 +/+ and 6 -/- per age
171 group). Heads were removed post-mortem and fixed in 10% neutral buffered formalin.
172 Genotype of mice was determined by isolating DNA from tail biopsies and PCR-based
173 detection of the wild type *Mstn* (+) and knock-out *Mstn* (-) alleles as described by Mendias et
174 al. (2006). Sex was confirmed using PCR probes against the *Sry* gene, which is located on
175 the Y chromosome.

176 *Imaging:* Each head was imaged twice. Once with standard microCT to capture the skull
177 geometry and subsequently with I₂KI (9% w/v) enhanced microCT to visualise the muscle
178 architecture (see Fig. 1 and Jeffery et al, 2011). Both sets were acquired using a SkyScan
179 1272 (Bruker Ltd) with 50Kv, 200uA and an aluminium filter. Vertices of the resulting
180 isometric voxels ranged from 26 to 40um. Contrast enhancement is associated with tissue
181 shrinkage (Vickerton et al., 2013). The method was standardised here so the effect is likely

182 to be the same for both groups and small given findings from similar whole mouse head
183 studies (e.g. Cox & Jeffery, 2011; Baverstock et al., 2013; Jeffery & Mendias, 2014).

184 *Morphometrics:* Masseter muscle and endocranial volumes were calculated using the
185 stereological method implemented in VolumEst (v2010) for ImageJ (v1.51p). The
186 endocranium is a reliable proxy for the brain in a range of craniates, including mammals (e.g.
187 Dumoncel et al., 2020; Early et al., 2020). Relative masseter size was calculated as
188 masseter volume divided by endocranial volume. Skull centroid size was calculated as the
189 square root of the sum of squared distances between the landmarks shown in Figure 2a.
190 Bivariate plots with local estimated scatterplot smoothing (LEOSS) and boxplots with
191 Wilcoxon comparisons of -/- and +/- means were created in R (version 3.6.2). Three-
192 dimensional co-ordinates for a configuration of 18 reliable and readily identifiable skull
193 landmarks (Fig. 2a) were collected using the mark-up function in 3DSlicer (v4.10.1). This
194 configuration was chosen to provide reasonable morphological representation whilst keeping
195 the dimensionality of the shape space ($3L-7 = 47$) proportionate to the sample size (48) (see
196 Bookstein, 2017, 2019; Cardini, 2019; Cardini et al, 2019). Geometric morphometric
197 variations of the configuration of landmarks were investigated in MorphoJ (v1.07a) following
198 the principles and methods outlined by Drake & Klingenberg (2008) and Klingenberg (2016).
199 Allometric (size) related shape changes were investigated using a multivariate regression of
200 symmetric Procrustes coordinates against log-transformed centroid size. Residuals from this
201 regression were explored for nonallometric shape changes. Differences across age cohorts
202 and experimental groups were evaluated in MorphoJ with Canonical Variate Analysis (CVA)
203 and Discriminative Functions of Procrustes coordinates. Warped surfaces were created in
204 Landmark (version 3.0) with reference to the co-ordinates generated by MorphoJ. For
205 convenience, we illustrated the distribution of simulated forms within their own shape space
206 using a Principal Components Analysis (PCA) of the covariance matrix and crossed checked
207 findings against those generated by mesh deformations (see below).

208 *Computational simulation:* Deformations of the skull due to endocranial and muscle
209 enlargement were simulated *in-silico* using a mass exchange gradient finite element
210 approach (see Ateshian et al 2009). Co-registered standard and contrast enhanced microCT
211 data (Fig. 2b) for the control (+/+) 28 day mouse closest to the mean shape (specimen
212 M1C1) were used to reconstruct, refine and mesh a model of the skull, mandible and
213 masticatory muscles (masseter, temporalis and pterygoids) in Amira version 5.4.1 (Thermo
214 Fisher Scientific Ltd, Waltham, Massachusetts, USA). The final decimated tetrahedral mesh,
215 which consisted of 1.3 million elements (Fig. 2c), was imported into FEBio version 2.8.2
216 (Maas et al., 2012) and parameterised. The simulation was simplified by assuming the skull
217 was a structural continuum and that skull elasticity was invariant spatially as well as for the

218 duration of the simulation. The mandibular incisors were used as rigid body constraints, and
219 the mass exchange gradients representing constituent materials were adjusted to achieve
220 the desired volumetric changes relative to the baseline +/+ model ($S_{+/+}$). One model was
221 created to simulate the 28 day -/- condition ($S_{-/-}$). In this case, the $S_{+/+}$ baseline model
222 elastically deforms to accommodate a computationally driven 7% reduction of endocranial
223 volume and 17% increase of masticatory muscle volume. This was repeated without the
224 endocranial reduction (M_{+17}). The remaining simulations were used to explore shape
225 changes associated with theoretical expansion of the muscles and endocranium (see Table
226 1). The models were solved using a non-linear quasi-static method, landmarked and
227 incorporated into the shape analyses as outlined above. Whole mesh deformations were
228 also visualised in FEBio.

229 In all statistical comparisons a probability (p) value of ≤ 0.05 was used to identify the most
230 prominent differences. Although somewhat arbitrary and subject to recent criticism (e.g.
231 Amrhein et al., 2019), this threshold was appropriate for the purposes of this study on the
232 understanding that a $p > 0.05$ is not equivalent to no difference but can represent a weaker
233 effect compared with ≤ 0.05 .

234

235 **Results**

236 *Euclidean Morphometrics:* Bivariate plots against age with accompanying boxplots and
237 Wilcoxon p-values are given in Figures 3a-d. Endocranial volumes were larger in +/+ mice
238 from 1 through to 28 postnatal days (Fig3a). Masseter volumes were at first larger among
239 the +/+ mice (1 day), switching to larger among -/- mice at 7 and 28 days (Fig3b). By 28
240 days -/- masseters and endocrania were on average 17% larger and 7% smaller,
241 respectively. Both groups experienced increased relative masseter size (masseter
242 volume/endocranial volume) after day 7 (Fig. 3c). The increase was greater for -/- mice.
243 There was little difference of centroid size until 28 days, at which point +/+ mice were on
244 average 1.1mm larger (Fig 3d). These findings predict corresponding shifts of skull form to
245 accommodate relative masticatory muscle enlargement, and that such effects will be more
246 pronounced among the -/- mice.

247 *Geometric Morphometrics:* Regression (Fig. 4a) of the symmetric component of the
248 Procrustes co-ordinates (combined fit; $n=48$) suggests both -/- and +/+ mice follow a
249 common allometric trend against centroid size, which explains approximately 77% of the
250 total shape variation. Allometric changes from 1 to 28 days are illustrated in Figure 4b and
251 included relative: elongation of the palate; narrowing of the midface and calvarium; flattening
252 of the posterior cranial base and ventrodorsal shortening of the calvarium. Overall, the mean

253 skull shape representative of all 28day mice was relatively more compact and
254 dolichocephalic whilst the face was longer and deflected dorsally (airorhynchy).

255 Relative masseter size predicted 59% (p-value <0.001) of the shape variation from 1 to 28
256 days. It also predicted 17% of the shape variance after size correction (residuals of
257 regression against centroid size). Figure 3c suggested relative masseter enlargement
258 occurred after day 1. Limiting the current analyses to days 7 to 28 showed that relative
259 masseter size predicted 48% of the nonallometric shape variance (Figure 5a). Changes
260 described included relative lateral displacement of the zygomatic arches, elongation of the
261 face, as well as narrowing and ventrodorsal shortening of the neurocranium and slight dorsal
262 bending of the face and of the posterior cranial base (Fig.5b). These patterns were broadly
263 similar to the allometric shape changes shown in Figure 4b, reflecting shared groupings
264 according to development (age) as well as growth (size).

265 Canonical Variate Analysis (CVA) of size corrected data revealed partitioning of the
266 nonallometric shape space between -/- and +/+ mice across canonical variate 2, which
267 represented 19% of the total variance (Fig. 6a). Procrustes distances are given in Table 2.
268 Shape differences at 28 days shown in Figure 5b were drawn from a discriminative function
269 (Procrustes D = 0.0271, p=<0.0001; cross-validation 100% accurate assignment). The major
270 shape differences were lateral displacement of the arches and caudolateral expansion of the
271 neurocranium among the 28 day -/- mice. Also observed in -/- mice were a decrease of facial
272 height, particularly around the rostrum, and slight dorsal deflection of the palate.

273

274 *Simulations:* Computational simulations are summarised in Table 1. To evaluate our
275 approach, the simulations of the control model (S_{+/+}) and those approximating the -/-
276 condition at 28 days (S_{-/-} & M₊₁₇) were combined with the main dataset and the CVA reported
277 above was repeated. Figure 6c shows the equivalent plot including the control simulation
278 (S_{+/+}), which clusters with the 28 day +/+ mice. Shape differences described by the variates
279 are the same in both analyses. The simulated 17% muscle expansion (M₊₁₇) and muscle
280 expansion plus 7% endocranial reduction (S_{-/-}) models both cluster with the -/- mice (please
281 refer to Table 1 for abbreviations and conditions). These findings confirmed that simulations
282 broadly mimic actual shape differences observed between -/- and +/+ mice (see above) and
283 indicated that muscle enlargement rather than reduced endocranial growth had the greatest
284 influence on these shape differences.

285 The three empirically informed simulations (S_{+/+}, S_{-/-} & M₊₁₇) were then combined with
286 extended, theoretical, models of muscle and endocranial expansion (see Table 1) and
287 subjected to PCA. PC1 explained 94% of variance (Fig. 7a), representing mostly simulated

288 increases of masticatory muscle volume in one direction (+PC) and simulated increases of
289 endocranial volume in the other (-PC). Simulated enlargement of the masticatory muscles
290 was associated with lateral displacement of the zygomatic arches, dorsal deflection of the
291 face (airorhynchy), ventrodorsal shortening of the neurocranium, and retroflexion (flattening)
292 of the posterior cranial base (Fig. 7b). The opposite trend was seen with simulated
293 endocranial enlargement (Fig. 7c), which was characterised by basicranial flexion,
294 neurocranial enlargement and ventral deflection of the face (kyphosis or klinorhynchy). PC2
295 (6%) showed the combined effects of computationally driven muscle and endocranial
296 expansion. Findings indicate that muscle expansion limits endocranial induced flexion of the
297 posterior cranial base and endocranial expansion limits dorsal deflection of the face
298 associated with muscle enlargement (Fig. 7d). Whole mesh (1.3 million elements)
299 displacement vector plots (bottom row in Figs. 7b-d) revealed similar trends to the above
300 landmarked defined analyses. Endocranial expansion was primarily characterised by
301 neurocranial expansion as well as ventral deflection of the face and the cranial base,
302 including basicranial flexion (bottom row Fig. 7c). By contrast, muscle expansion was
303 primarily characterised dorsal deflection of the posterior neurocranium, face and cranial
304 base, including basicranial retroflexion, as well as lateral expansion of the zygomatic arches
305 (bottom row Fig. 7b). Combining the two simulated expansions, appears to redirect and
306 magnify the displacement posteriorly whilst constraining the flexion to basicranial elongation
307 and the extent of dorsal facial deflection (bottom row Fig. 7d). Lateral displacement of the
308 zygomatic arches remained.

309

310 **Discussion**

311 Compared with the controls (+/+), the 28-day old myostatin deficient (-/-) mice had on
312 average 17% larger masseters and 7% smaller endocrania, the latter being used here as a
313 proxy for brain size (see methods). A previous study by Jeffery & Mendias (2014) suggests
314 this pattern continues into later adulthood with differences of +43% and -16%, respectively in
315 mice aged 60 to 517 days (average 233 days). Similar increases of masseter size have been
316 reported before (see Vecchione et al., 2007 & 2010; Cray et al 2011). In particular, our
317 results corroborate those of Vecchione et al (2010) showing that day old +/+ mice have
318 larger masseters than -/- mice. These findings suggest that the hypermuscular phenotype
319 emerges after birth, during the first week of life, and then rapidly accelerates. By contrast,
320 the -/- mice had smaller endocrania from day one, which suggests the reduced brain size
321 occurred in-utero and preceded and then accompanied the accelerated muscle growth.
322 Thus, our findings do not corroborate the idea of muscularity directly constraining brain size

323 as implied by Stedman et al (2004). Indeed, that -/- endocrania are smaller at birth suggests
324 the involvement of more systemic factors.

325 Myostatin is known to be an important pre- and postnatal metabolic regulator (McPherron
326 and Lee, 2002; Guo et al, 2009; Ploquin et al, 2012; Carneiro et al, 2013; Mouisel et al,
327 2014) and has been shown to act as a communicative link between muscle and fat (Kong et
328 al, 2018; Deng et al, 2020). Deficiency may therefore limit the availability of lipids for myelin
329 formation, which can in turn impede intra-uterine brain growth (Bourre et al., 1981; Morand
330 et al., 1981). Myostatin deficiency may also have altered brain cell development. Since we
331 reported the reduced endocranial phenotype in 2014, several studies have reported the
332 abundant expression of myostatin-like proteins throughout the brain, including glia as well as
333 neurons (e.g. Hayashi et al, 2018; Schafer et al, 2019; Augustin et al., 2017). This suggests
334 myostatin is an important factor for neuronal growth and maintenance. We therefore contend
335 that the reduced -/- endocrania reported here and by Jeffery and Mendias (2014) are the
336 product of altered prenatal neuronal growth, possibly exacerbated by the metabolic demands
337 of growing and maintaining larger muscles later in life.

338 Rather than constraining brain size, our mouse data and more clearly our simulations
339 support the hypothesis that masticatory muscle enlargement limits the effects of brain
340 expansion on the surrounding skull. Most notably, masticatory muscle enlargement curbs
341 basicranial flexion, whilst brain enlargement in turn restricts some effects of muscle
342 enlargement such as dorsal deflection of the face (Biegert, 1963; see also Ross & Ravosa,
343 1993; Ross & Henneberg, 1995). The aim of our computational approach was not to
344 replicate the intricacies of the murine head but to simulate deformation driven by tissue
345 expansion. Realism could and should be enhanced in future models, albeit at the expense of
346 computational load and possibly stability. Refinements might include, for example, growth of
347 additional anatomical modules such as the eyes and extraocular apparatus (e.g. Ross &
348 Kirk, 2007; Jeffery et al., 2007), nuchal musculature and nasal turbinates as well as the face
349 (Bastir et al., 2010), the pharynx (e.g. Jeffery, 2005) and the nasal septum (Jeffery et al.,
350 2007). Adding ontogenetic shifts of skull compliance will be particularly enlightening,
351 especially changes related to the formation of ossification centres and the subsequent
352 localisation of deformation to, and eventual fusion of, sutures and synchondroses (see
353 Michejda, 1972; Jeffery & Spoor, 2004; Oladipupo et al., 2020). Whilst adding such
354 complexity will no doubt provide more detail and nuance (see for example Lee &
355 Richtsmeier, 2019), it is remarkable nonetheless how much of the *in-vivo* changes were
356 captured here *in-silico* on the basis of simply tissue expansion and elastic deformation.
357 Mechanical deformation appears to mirror the effects of mechanisms underlying ontogeny of
358 the murine skull and is perhaps a precursor or adjunct to physiological tissue (re)modelling.

359 From these and previous findings we can infer the variegated and phasic nature of skull
360 ontogeny (see also Bastir and Rosas 2016; Zollikofer et al. 2017). We know that
361 morphogenetic covariations predominate during embryogenesis. Presumably, these trends
362 remain coherent for most of prenatal life, reflecting the residual power of the genes involved
363 as well as relatively relaxed functional demands and spatial constraints. For example,
364 consider the fetus suspended in amniotic fluid, nourished via the umbilical cord and with a
365 flexible, membranous, calvarium. Recent in-utero MR images have also shown a
366 comfortable margin of cerebrospinal fluid surrounding the brain, which could be displaced via
367 arachnoid granulations to lessen the physical effects of encephalisation on the surrounding
368 skull (see figures in Jarvis et al, 2019; Kyriakopoulou et al., 2017). In other words, the head
369 is not yet spatially optimised at this stage and retains capacity to accommodate expanding
370 tissues. However, as ontogeny proceeds, the genetic signals lose coherence, developmental
371 noise accumulates and tissues become increasingly crowded and sculpted by functional
372 demands like mastication. At this point, the established spatial arrangement of tissues,
373 referred to here as heterotopy, would be distorted by greater competition for space as
374 modules adopt distinct allometric trajectories and disperse along different heterochronic
375 timelines (see Zelditch & Fink 1996; Zollikofer & Ponce De León, 2004). This supposition,
376 which is summarised in Figure 8, might help explain why investigations of spatial-packing
377 using fetal samples (e.g. Jeffery & Spoor, 2002 & 2004; Jeffery, 2003; Jeffery et al., 2007)
378 have seemingly contradicted adult studies (e.g. Ross & Ravosa, 1993; Ross & Henneberg,
379 1995; Veneziano et al. 2019; Neaux et al., 2015). Indeed, whilst it pains at least one of us
380 (NJ) to concede, it appears that spatial-packing like phenomena are best detected later in
381 ontogeny and possibly in differences among the adult, spatially optimised, endpoints rather
382 than along intraspecific prenatal ontogenies. The above paradigm also emphasises the
383 importance of considering the protean mix of sources as well as the resulting patterns of
384 covariation in studies of morphological integration and modularity over ontogenetic time
385 (Klingenberg, 2008; 2014), and supports the case for explicitly recognising spatial-packing
386 like covariations linked to heterotopy in the various theoretical frameworks that govern such
387 studies and our current understanding of mammalian skull development.

388

389 **Acknowledgements**

390 The authors would like to thank the many developers involved in creating and maintaining
391 FEBio (www.febio.org), R (www.r-project.org), 3Dslicer (www.slicer.org) as well as MorphoJ
392 (www.morphometrics.uk) and ImageJ (imagej.nih.gov). Without their support this research
393 would not have been financially viable. We also thank two reviewers for their comments and

394 suggestions. Thanks to their input, the final version of this manuscript is a significant
395 improvement on the original submitted.

396

397 **Conflicts of Interest**

398 None declared

399 **Data availability statement**

400 All relevant data are presented in the results section and figures.

401

402

403

404 **ORCID**

405 Nathan Jeffery <https://orcid.org/0000-0001-5166-2029>

406 Christopher Mendias <https://orcid.org/0000-0002-2384-0171>

407

408

409 **References**

410 Amrhein, V., Greenland, S., & McShane, B. (2019). Comment: Retire statistical significance.
411 *Nature*, 567, 305-307.

412 Anderson, P. S., Renaud, S., & Rayfield, E. J. (2014). Adaptive plasticity in the mouse
413 mandible. *BMC Evolutionary Biology*, 14(1), 85.

414 Anthony, R. (1903). Introduction à l'étude expérimentale de la morphogénie. *Bulletins et*
415 *Mémoires de la Société d'Anthropologie de Paris*, 4(1), 119-145.

416 Ateshian, G. A., Costa, K. D., Azeloglu, E. U., Morrison, B., & Hung, C. T. (2009). Continuum
417 modeling of biological tissue growth by cell division, and alteration of intracellular osmolytes
418 and extracellular fixed charge density. *Journal of biomechanical engineering*, 131(10),
419 101001.

420 Augustin, H., McGourty, K., Steinert, J. R., Cochemé, H. M., Adcott, J., Cabecinha, M., &
421 Partridge, L. (2017). Myostatin-like proteins regulate synaptic function and neuronal
422 morphology. *Development*, 144(13), 2445-2455.

- 423 Bastir, M., Rosas, A., Stringer, C., Cuétara, J. M., Kruszynski, R., Weber, G. W., ... &
424 Ravosa, M. J. (2010). Effects of brain and facial size on basicranial form in human and
425 primate evolution. *Journal of Human Evolution*, 58(5), 424-431.
- 426 Bastir M, and Rosas A. 2016. Cranial base topology and basic trends in the facial evolution
427 of Homo. *Journal of Human Evolution* 91:26-35.
- 428 Baverstock, H., Jeffery, N. S., & Cobb, S. N. (2013). The morphology of the mouse
429 masticatory musculature. *Journal of Anatomy*, 223(1), 46-60.
- 430 Biegert, J. (1963). The evaluation of characteristics of the skull, hands and feet for primate
431 taxonomy. In *Classification and human evolution* (Vol. 37, pp. 116-145). Aldine Chicago.
- 432 Bookstein, F. L. (2017). A newly noticed formula enforces fundamental limits on geometric
433 morphometric analyses. *Evolutionary Biology*, 44(4), 522-541.
- 434 Bookstein, F. L. (2019). Pathologies of between-groups principal components analysis in
435 geometric morphometrics. *Evolutionary Biology*, 46(4), 271-302.
- 436 Bourre, J. M., Morand, O., Chanez, C., Dumont, O., & Flexor, M. A. (1981). Influence of
437 intrauterine malnutrition on brain development: alteration of myelination. *Neonatology*, 39(1-
438 2), 96-99.
- 439 Byron, C. D., Hamrick, M. W., & Wingard, C. J. (2006). Alterations of temporalis muscle
440 contractile force and histological content from the myostatin and Mdx deficient mouse.
441 *Archives of oral biology*, 51(5), 396-405.
- 442 Cardini, A. (2019). Integration and modularity in Procrustes shape data: is there a risk of
443 spurious results?. *Evolutionary Biology*, 46(1), 90-105.
- 444 Cardini, A., O'Higgins, P., & Rohlf, F. J. (2019). Seeing distinct groups where there are none:
445 spurious patterns from between-group PCA. *Evolutionary Biology*, 46(4), 303-316.
- 446 Carneiro, I., González, T., López, M., Señarís, R., Devesa, J., & Arce, V. M. (2013).
447 Myostatin expression is regulated by underfeeding and neonatal programming in rats.
448 *Journal of physiology and biochemistry*, 69(1), 15-23.

449 Cox, P. G., & Jeffery, N. (2011). Reviewing the morphology of the jaw-closing musculature in
450 squirrels, rats, and guinea pigs with contrast-enhanced microCT. *The Anatomical Record:*
451 *Advances in Integrative Anatomy and Evolutionary Biology*, 294(6), 915-928.

452 Cray Jr, J., Kneib, J., Vecchione, L., Byron, C., Cooper, G. M., Losee, J. E., ... & Mooney, M.
453 P. (2011). Masticatory HyperMuscularity is not Related to Reduced Cranial Volume in
454 Myostatin-Knockout Mice. *The Anatomical Record: Advances in Integrative Anatomy and*
455 *Evolutionary Biology*, 294(7), 1170-1177.

456 Deng, B., Zhang, F., Wen, J., Shen, W., Gao, Q., Peng, X., ... & Liu, W. (2020). The
457 transcriptomes from two adipocyte progenitor cell types provide insight into the differential
458 functions of MSTN. *Genomics*.

459 Drake, A. G., & Klingenberg, C. P. (2008). The pace of morphological change: historical
460 transformation of skull shape in St Bernard dogs. *Proceedings of the Royal Society B:*
461 *Biological Sciences*, 275(1630), 71-76.

462 Dumoncel, J., Subsol, G., Durrleman, S., Bertrand, A., de Jager, E., Oettlé, A. C., ... &
463 Beaudet, A. (2020). Are endocasts reliable proxies for brains? A 3D quantitative comparison
464 of the extant human brain and endocast. *Journal of Anatomy*

465 Early, C. M., Iwaniuk, A. N., Ridgely, R. C., & Witmer, L. M. (2020). Endocast structures are
466 reliable proxies for the sizes of corresponding regions of the brain in extant birds. *Journal of*
467 *Anatomy*.

468 Edamoto, M., Kuroda, Y., Yoda, M., Kawaai, K., & Matsuo, K. (2019). Trans-pairing between
469 osteoclasts and osteoblasts shapes the cranial base during development. *Scientific reports*,
470 9(1), 1-11.

471 Enlow, D. H. (1962). A study of the post-natal growth and remodeling of bone. *American*
472 *Journal of Anatomy*, 110(2), 79-101.

473 Green, R. M., Fish, J. L., Young, N. M., Smith, F. J., Roberts, B., Dolan, K., ... & Roseman,
474 C. C. (2017). Developmental nonlinearity drives phenotypic robustness. *Nature*
475 *communications*, 8(1), 1970.

476 Goswami, A., Binder, W. J., Meachen, J., & O'Keefe, F. R. (2015). The fossil record of
477 phenotypic integration and modularity: A deep-time perspective on developmental and

478 evolutionary dynamics. *Proceedings of the National Academy of Sciences*, 112(16), 4891-
479 4896.

480 Gould, S. J. (2002). *The structure of evolutionary theory*. Harvard University Press.

481 Guo, T., Jou, W., Chanturiya, T., Portas, J., Gavrilova, O., & McPherron, A. C. (2009).
482 Myostatin inhibition in muscle, but not adipose tissue, decreases fat mass and improves
483 insulin sensitivity. *PLoS one*, 4(3), e4937.

484 Hayashi, Y., Mikawa, S., Ogawa, C., Masumoto, K., Katou, F., & Sato, K. (2018). Myostatin
485 expression in the adult rat central nervous system. *Journal of chemical neuroanatomy*, 94,
486 125-138.

487 Jarvis, D. A., Finney, C. R., & Griffiths, P. D. (2019). Normative volume measurements of the
488 fetal intra-cranial compartments using 3D volume in utero MR imaging. *European radiology*,
489 29(7), 3488-3495.

490 Jeffery, N. (2003). Brain expansion and comparative prenatal ontogeny of the non-hominoid
491 primate cranial base. *Journal of human evolution*, 45(4), 263-284.

492 Jeffery, N. (2005). Cranial base angulation and growth of the human fetal pharynx. *The*
493 *Anatomical Record Part A: Discoveries in Molecular, Cellular, and Evolutionary Biology: An*
494 *Official Publication of the American Association of Anatomists*, 284(1), 491-499.

495 Jeffery, N., Davies, K., Köckenberger, W., & Williams, S. (2007). Craniofacial growth in fetal
496 *Tarsius bancanus*: brains, eyes and nasal septa. *Journal of anatomy*, 210(6), 703-722.

497 Jeffery, N., & Mendias, C. (2014). Endocranial and masticatory muscle volumes in
498 myostatin-deficient mice. *Royal Society open science*, 1(4), 140187.

499 Jeffery, N., & Spoor, F. (2002). Brain size and the human cranial base: a prenatal
500 perspective. *American journal of physical anthropology*, 118(4), 324.

501 Jeffery, N., & Spoor, F. (2004). Ossification and midline shape changes of the human fetal
502 cranial base. *American Journal of Physical Anthropology*, 123(1), 78-90.

503 Jeffery, N. S., Stephenson, R. S., Gallagher, J. A., Jarvis, J. C., & Cox, P. G. (2011). Micro-
504 computed tomography with iodine staining resolves the arrangement of muscle fibres.
505 *Journal of biomechanics*, 44(1), 189-192.

- 506 Kappers, C. A. (1932). The David Ferrier Lecture: On Some Correlations between Skull and
507 Brain. *Philosophical Transactions of the Royal Society of London. Series B, Containing*
508 *Papers of a Biological Character*, 391-429.
- 509 Klingenberg, C. P. (2008). Morphological integration and developmental modularity. *Annual*
510 *review of ecology, evolution, and systematics*, 39, 115-132.
- 511 Klingenberg, C. P. (2014). Studying morphological integration and modularity at multiple
512 levels: concepts and analysis. *Philosophical Transactions of the Royal Society B: Biological*
513 *Sciences*, 369(1649), 20130249.
- 514 Klingenberg, C. P. (2016). Size, shape, and form: concepts of allometry in geometric
515 morphometrics. *Development genes and evolution*, 226(3), 113-137.
- 516 Kong, X., Yao, T., Zhou, P., Kazak, L., Tenen, D., Lyubetskaya, A., ... & Liu, T. (2018).
517 Brown adipose tissue controls skeletal muscle function via the secretion of myostatin. *Cell*
518 *metabolism*, 28(4), 631-643.
- 519 Kyriakopoulou, V., Vatansever, D., Davidson, A., Patkee, P., Elkommos, S., Chew, A., ... &
520 Fox, M. (2017). Normative biometry of the fetal brain using magnetic resonance imaging.
521 *Brain Structure and Function*, 222(5), 2295-2307.
- 522 Lahti, D. C., Johnson, N. A., Ajie, B. C., Otto, S. P., Hendry, A. P., Blumstein, D. T., ... &
523 Foster, S. A. (2009). Relaxed selection in the wild. *Trends in ecology & evolution*, 24(9), 487-
524 496.
- 525 Laland, K. N., Uller, T., Feldman, M. W., Sterelny, K., Müller, G. B., Moczek, A., ... & Odling-
526 Smee, J. (2015). The extended evolutionary synthesis: its structure, assumptions and
527 predictions. *Proceedings of the Royal Society B: Biological Sciences*, 282(1813), 20151019.
- 528 Lee, C., Richtsmeier, J. T., & Kraft, R. H. (2019). A coupled reaction–diffusion–strain model
529 predicts cranial vault formation in development and disease. *Biomechanics and modeling in*
530 *mechanobiology*, 1-15.
- 531 Lesciotto, K. M., & Richtsmeier, J. T. (2019). Craniofacial skeletal response to
532 encephalization: How do we know what we think we know?. *American journal of physical*
533 *anthropology*, 168, 27-46.

- 534 Lieberman, D. E., Ross, C. F., & Ravosa, M. J. (2000). The primate cranial base: ontogeny,
535 function, and integration. *American Journal of Physical Anthropology: The Official*
536 *Publication of the American Association of Physical Anthropologists*, 113(S31), 117-169.
- 537 Maas, S. A., Ellis, B. J., Ateshian, G. A., & Weiss, J. A. (2012). FEBio: finite elements for
538 biomechanics. *Journal of biomechanical engineering*, 134(1), 011005.
- 539 McPherron, A. C., & Lee, S. J. (2002). Suppression of body fat accumulation in myostatin-
540 deficient mice. *The Journal of clinical investigation*, 109(5), 595-601.
- 541 Mendias, C. L., Marcin, J. E., Calerdon, D. R., & Faulkner, J. A. (2006). Contractile
542 properties of EDL and soleus muscles of myostatin-deficient mice. *Journal of applied*
543 *physiology*, 101(3), 898-905.
- 544 Michejda, M. (1972). The role of basicranial synchondroses in flexure processes and
545 ontogenetic development of the skull base. *American Journal of Physical Anthropology*,
546 37(1), 143-150.
- 547 Morand, O., Chanez, C., Masson, M., Dumont, O., Flexor, M. A., Baumann, N., & Bourre, J.
548 M. (1981). Intrauterine growth retardation (malnutrition by vascular ligation) induces
549 modifications in fatty acid composition of neurons and oligodendrocytes. *Journal of*
550 *neurochemistry*, 37(4), 1057-1060.
- 551 Moss, M. L. & Young, R. W. A functional approach to craniology. *American Journal of*
552 *Physical Anthropology* 281-92 (1960)
- 553 Mouisel, E., Relizani, K., Mille-Hamard, L., Denis, R., Hourdé, C., Agbulut, O., ... & Garcia, L.
554 (2014). Myostatin is a key mediator between energy metabolism and endurance capacity of
555 skeletal muscle. *American Journal of Physiology-Regulatory, Integrative and Comparative*
556 *Physiology*, 307(4), R444-R454.
- 557 Murren, C. J., Auld, J. R., Callahan, H., Ghalambor, C. K., Handelsman, C. A., Heskell, M. A.,
558 & Pfennig, D. W. (2015). Constraints on the evolution of phenotypic plasticity: limits and
559 costs of phenotype and plasticity. *Heredity*, 115(4), 293.
- 560 Neaux, D., Gilissen, E., Coudyzer, W., & Guy, F. (2015). Integration between the face and
561 the mandible of Pongo and the evolution of the craniofacial morphology of orangutans.
562 *American journal of physical anthropology*, 158(3), 475-486.

- 563 Neubauer, G. (1925). Experimentelle Untersuchungen über die Beeinflussung der
564 Schädelform. *Zeitschrift für Morphologie und Anthropologie*, (H. 3), 411-442.
- 565 Oladipupo, L., Wood, B., Mano, N., Hughes, G., Reynolds, R., Vinyard, C., ... & Smith, T.
566 (2020). Development of basicranium in cotton-top tamarin compared to the development of
567 basicranium in bushbabies: Role of synchondroses and brain growth. *The FASEB Journal*,
568 34(S1), 1-1.
- 569 Ploquin, C., Chabi, B., Fouret, G., Vernus, B., Feillet-Coudray, C., Coudray, C., ... &
570 Ramonatxo, C. (2012). Lack of myostatin alters intermyofibrillar mitochondria activity,
571 unbalances redox status, and impairs tolerance to chronic repetitive contractions in muscle.
572 *American journal of physiology-Endocrinology and metabolism*, 302(8), E1000-E1008.
- 573 Ross, C. F. & Henneberg, M. (1995). Basicranial flexion, relative brain size and facial
574 kyphosis in *Homo sapiens* and some fossil hominids. *American Journal of Physical*
575 *Anthropology* **98**, 575-593.
- 576 Ross, C. F., & Kirk, E. C. (2007). Evolution of eye size and shape in primates. *Journal of*
577 *Human Evolution*, 52(3), 294-313.
- 578 Ross, C. F. & Ravosa, M. J. (1993). Basicranial flexion, relative brain size, and facial
579 kyphosis in nonhuman primates. *American Journal of Physical Anthropology* **91**, 305-324.
- 580 Schafer, M. J., & LeBrasseur, N. K. (2019). The influence of GDF11 on brain fate and
581 function. *GeroScience*, 41(1), 1-11.
- 582 Singleton, M. (2013) Primate Cranial Diversity. *Nature Education Knowledge* 4(12):1
- 583 Stedman, H. H., Kozyak, B. W., Nelson, A., Thesier, D. M., Su, L. T., Low, D. W., ... &
584 Mitchell, M. A. (2004). Myosin gene mutation correlates with anatomical changes in the
585 human lineage. *Nature*, 428(6981), 415.
- 586 Stewart, S., Darwood, A., Masouros, S., Higgins, C., & Ramasamy, A. (2020).
587 Mechanotransduction in osteogenesis. *Bone & Joint Research*, 9(1), 1-14.
- 588 Vecchione, L., Miller, J., Byron, C., Cooper, G. M., Barbano, T., Cray, J., ... & Mooney, M. P.
589 (2010). Age-related changes in craniofacial morphology in GDF-8 (myostatin)-deficient mice.
590 *The Anatomical Record: Advances in Integrative Anatomy and Evolutionary Biology*, 293(1),
591 32-41.

592 Vecchione, L., Byron, C., Cooper, G. M., Barbano, T., Hamrick, M. W., Sciote, J. J., &
593 Mooney, M. P. (2007). Craniofacial morphology in myostatin-deficient mice. *Journal of dental*
594 *research*, 86(11), 1068-1072.

595 Veneziano, A., Meloro, C., Irish, J. D., Stringer, C., Profico, A., & De Groote, I. (2018).
596 Neuromandibular integration in humans and chimpanzees: Implications for dental and
597 mandibular reduction in Homo. *American journal of physical anthropology*, 167(1), 84-96.

598 Vickerton, P., Jarvis, J., & Jeffery, N. (2013). Concentration-dependent specimen shrinkage
599 in iodine-enhanced micro CT. *Journal of anatomy*, 223(2), 185-193.

600 Vincent, T. L., & Wann, A. K. (2019). Mechanoadaptation: articular cartilage through thick
601 and thin. *The Journal of physiology*, 597(5), 1271-1281.

602 Weidenreich, F. (1941). The brain and its role in the phylogenetic transformation of the
603 human skull. *Transactions of the American Philosophical Society*, 320-442.

604 Weiss, P. (1933). Functional adaptation and the role of ground substances in development.
605 *The American Naturalist*, 67(711), 322-340.

606 Williams, S. H., Lozier, N. R., Montuelle, S. J., & de Lacalle, S. (2015). Effect of postnatal
607 myostatin inhibition on bite mechanics in mice. *Plos one*, 10(8), e0134854.

608 Wolff, J. (1893). Das gesetz der transformation der knochen. *DMW-Deutsche Medizinische*
609 *Wochenschrift*, 19(47), 1222-1224.

610 Zheng, J., Payne, J. L., & Wagner, A. (2019). Cryptic genetic variation accelerates evolution
611 by opening access to diverse adaptive peaks. *Science*, 365(6451), 347-353.

612 Zelditch, M. L., & Fink, W. L. (1996). Heterochrony and heterotopy: stability and innovation in
613 the evolution of form. *Paleobiology*, 22(2), 241-254.

614 Zollikofer, C. P. E., & Ponce De León, M. S. (2004). Kinematics of cranial ontogeny:
615 heterotopy, heterochrony, and geometric morphometric analysis of growth models. *Journal*
616 *of Experimental Zoology Part B: Molecular and Developmental Evolution*, 302(3), 322-340.

617 Zollikofer CPE, Bienvenu T, and Ponce de León MS. 2017. Effects of cranial integration on
618 hominid endocranial shape. *Journal of anatomy* 230(1):85-105.

619

620

621 **Tables**

622

623 Table 1. Computationally driven changes of muscle and endocranial volume based on a
624 28day control (+/+) mouse mesh.

| Simulation ID | Δ Muscle Volume % | Δ Endocranial Volume % |
|---------------------------------------|--------------------------|-------------------------------|
| S_{+/+} | 0 | 0 |
| S_{-/-} | +17 | -7 |
| M₊₁₀ | +10 | 0 |
| M₊₁₇ | +17 | 0 |
| M₊₂₃ | +23 | 0 |
| E₊₁₁ | 0 | +11 |
| E₊₂₀ | 0 | +20 |
| E₊₃₀ | 0 | +30 |
| M₊₆E₊₅ | +6 | +5 |
| M₊₁₀E₊₉ | +10 | +9 |
| M₊₂₇E₊₂₁ | +27 | +21 |

625 S_{+/+} and S_{-/-} represent the +/+ and -/- conditions, respectively. Remaining models simulate
626 the combined and separate effects of muscle and endocranial expansion

627

628

629

630

631 Table 2. Myostatin -/- versus +/+ canonical variate analysis (1000 permutations) based on
632 size corrected Procrustes data.

| Age Grp (days) | N | Procrustes Distance † | Permutation p-value |
|-----------------------|----------|------------------------------|----------------------------|
| 1 | 12 | 0.0256 | 0.0101 |
| 7 | 12 | 0.0189 | 0.0008 |
| 14 | 12 | 0.0273 | 0.0014 |
| 28 | 12 | 0.0271 | 0.0020 |

633 † distance between +/+ and -/- mice

634

635 **Figure legends**

636

637 **Figure 1.** Example I₂KI enhanced microCT images reformatted along the midsagittal plane
638 at postnatal day 1, 7, 14 and 28. Scale bar 5mm.

639

640 **Figure 2.** Reformatted and rendered image data showing: **a)** from top to bottom, dorsal,
641 lateral and midline views of the landmark configuration superimposed on 3D isosurfaces (Ba,
642 basion; Br, bregma; Ef, ethmoid foramen; Fnt, junction between zygomatic, frontal and
643 premaxillary bones; Iss, intersphenoidal synchondrosis; Ld, lambda; Na, nasion; Op,
644 opisthion; Pl, posteriormost point of palatine suture; Pr, prosthion; Rs, recess above post-
645 tympanic hook; Ses, sphenoid-ethmoidal synchondrosis; Sos, sphenoid-occipital
646 synchondrosis; Zm, dorsal margin of zygomaticomaxillary suture); **b)** from left to right,
647 standard coronal microCT scan, I₂KI enhanced coronal microCT scan and the corresponding
648 composite label mapping; **c)** tetrahedral 3D mesh of mouse M1C1 used to create
649 simulations (bone, purple; muscle, yellow; endocranium, not shown; green & pink,
650 constraint).

651

652 **Figure 3.** Bivariate plots with LEOSS fits against age (standard error, grey) and boxplot
653 comparisons between +/+ (green) and -/- (blue) mice at 1, 7, 14 and 28 postnatal days for
654 measures of **a)** masseter volume; **b)** endocranial volume; **c)** relative masseter size
655 (masseter volume/endocranial volume); **d)** centroid size. Boxplots show the 25th, 50th & 75th
656 percentiles with hinges for datum points within 1.5 times the percentile range (p-values are
657 for Wilcoxon tests between +/+ and -/- means).

658

659 **Figure 4.** Size (allometric) related changes of craniofacial shape: **a)** bivariate plot of
660 regression scores from the Procrustes form space against log centroid size illustrating the
661 common allometric trend through the age groups of -/- and +/+ mice; **b)** surface renderings
662 representing the allometric trend from the mean day 1 mouse shape (rose) to the mean day
663 28 shape (green).

664

665 **Figure 5.** Size corrected (nonallometric) related changes of craniofacial shape in relation to
666 relative masseter size from 7 to 28 days: **a)** bivariate plot of nonallometric regression scores
667 against relative masseter size, accounting for 48% of the size corrected shape variation; **b)**
668 surface renderings representing size corrected shape variation associated with increases of
669 relative masseter size from 7 (yellow) to 28 days (red).

670

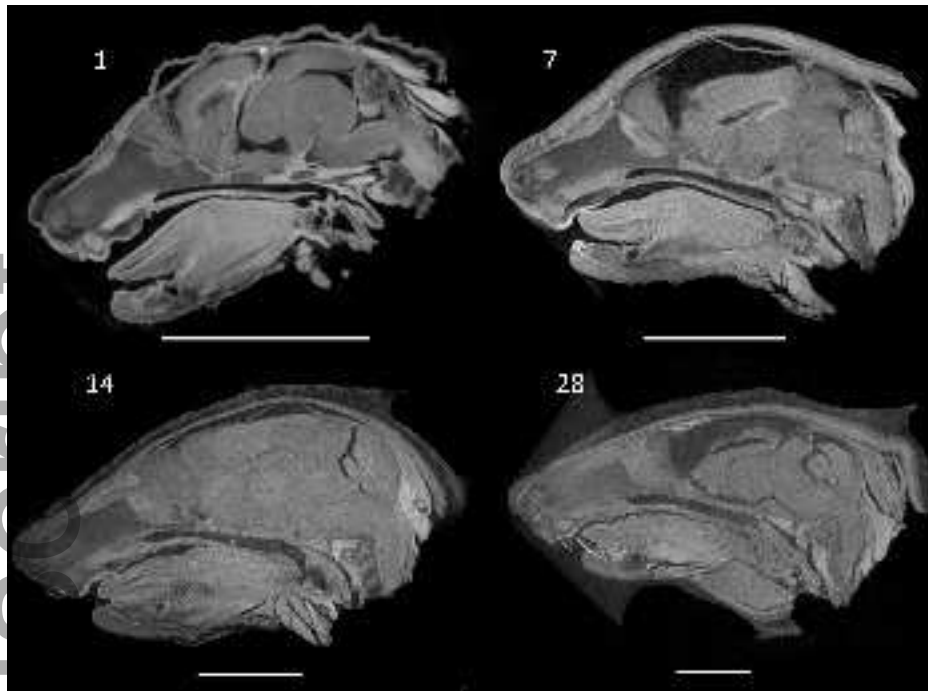
671 **Figure 6.** Nonallometric differences between -/- and +/+ mice: **a)** Plot of canonical variate
672 scores showing the partial separation of age groups along CV1 and separation of -/- & +/+
673 mice along CV2; **b)** 3D renderings representing nonallometric shape differences between
674 MSTN-/- and +/+ mice at day 28 based on a discriminative function; **c)** plot of canonical
675 variate scores including simulations (refer to Table 1 for abbreviations);

676

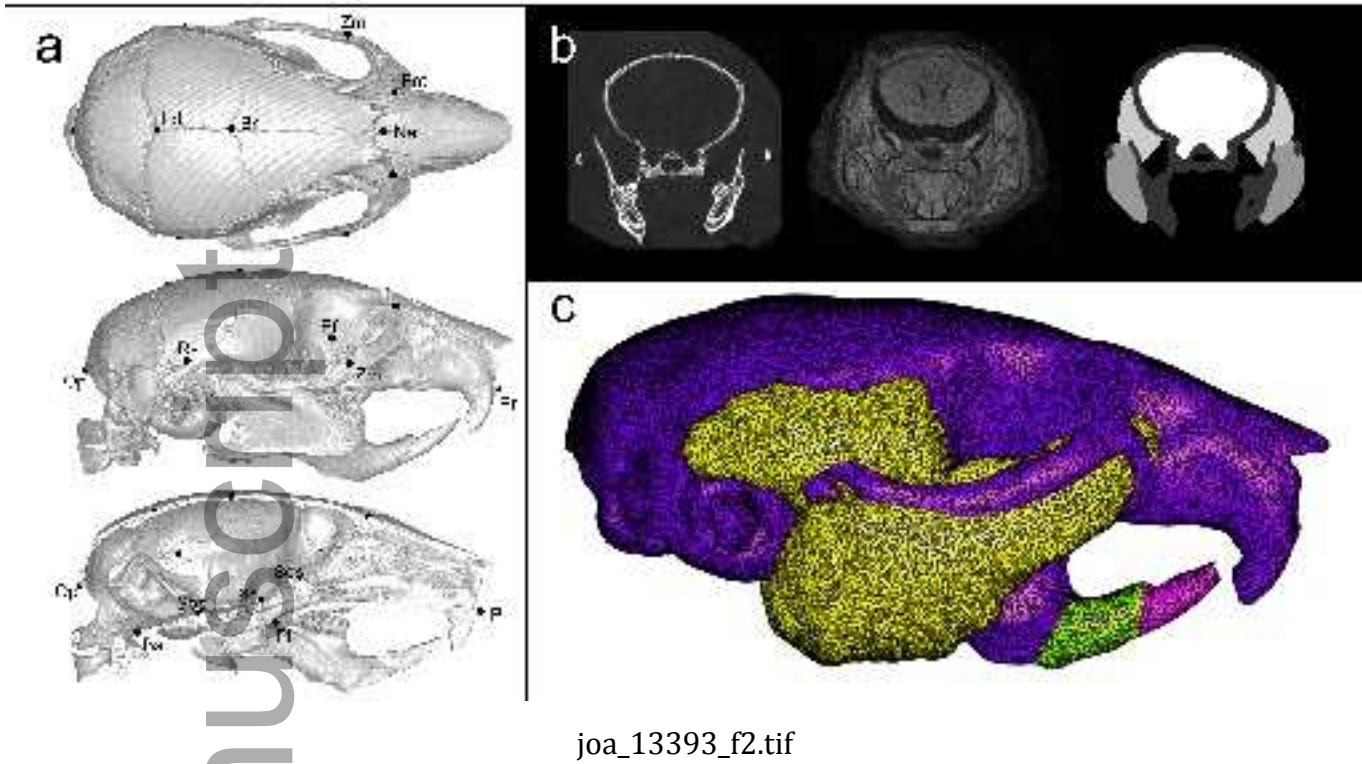
677 **Figure 7.** Soft-tissue expansion simulations; **a)** plot showing the distribution of simulated
678 skulls along principal components 1 and 2 of the shape space (refer to Table 1 for
679 abbreviations). Note that simulated muscle (e.g. M_{+17}) expansions are primarily distributed
680 along positive PC1 scores whereas simulated endocranial expansions (e.g. E_{+20}) fall along
681 the negative PC1 scores. Combined muscle and endocranial expansions (e.g. $M_{+27}E_{+21}$) fall
682 along PC2; **b-d)** 3D renderings of the corresponding shape changes (± 0.05 PC scale
683 factor) from the mean control shape ($S_{+/+}$, light blue) to the simulated shape (**b**, green
684 represents expanded muscle [M_{+23}]; **c**, rose represents expanded endocranium [E_{+30}]; **d**,
685 purple represents combined expansion of muscle and endocranium [$M_{+27}E_{+21}$]).
686 Accompanying colour mapped 3D renderings illustrate the corresponding mesh
687 deformations (red, high deformation; blue, low deformation; arrows also indicate direction
688 and magnitude [arrow length] of deformation).

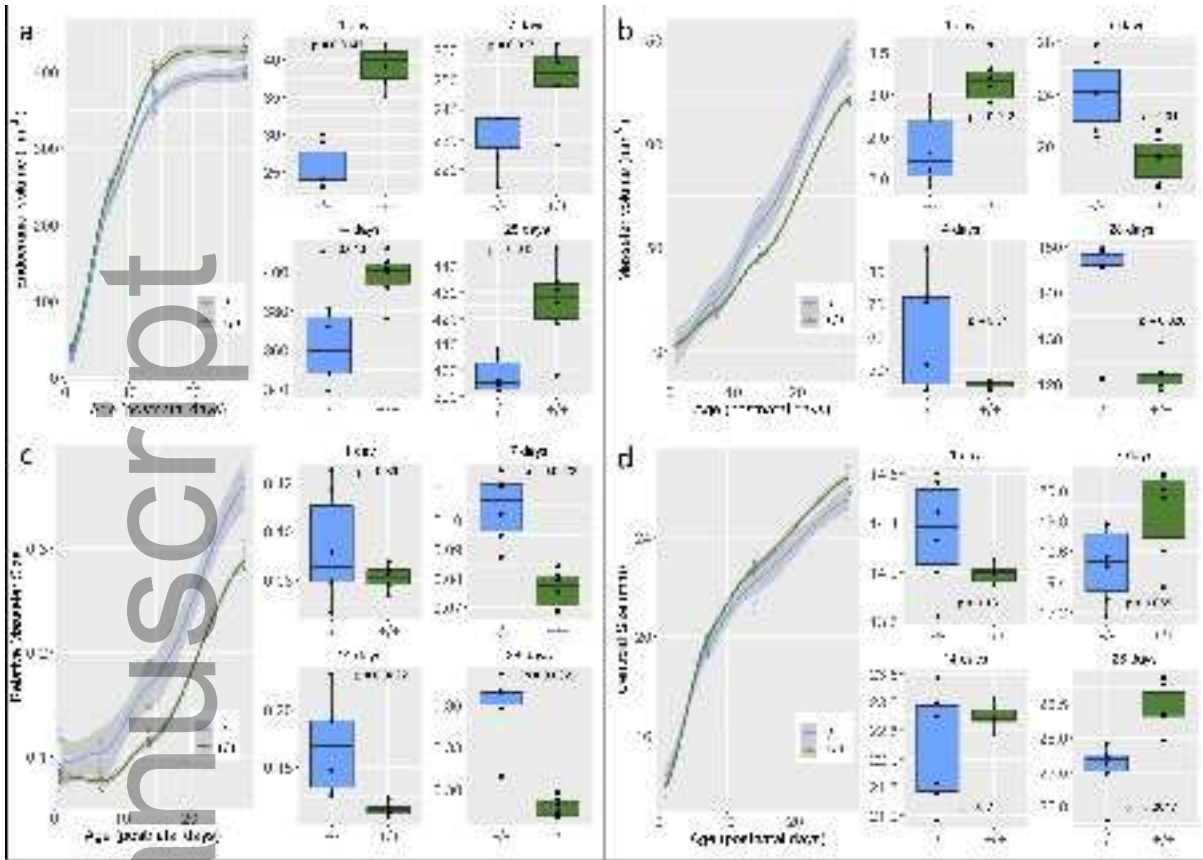
689

690 **Figure 8.** Diagrammatic representation of gene derived covariations of form manifested
691 through heterochrony (timing), allometry (size) and heterotopy (location). As ontogeny
692 progresses, these covariations lose coherence (broken green lines) and other sources (black
693 lines) such as the competition for space between nearby enlarging structures (heterotopy-
694 allometry) become more conspicuous.

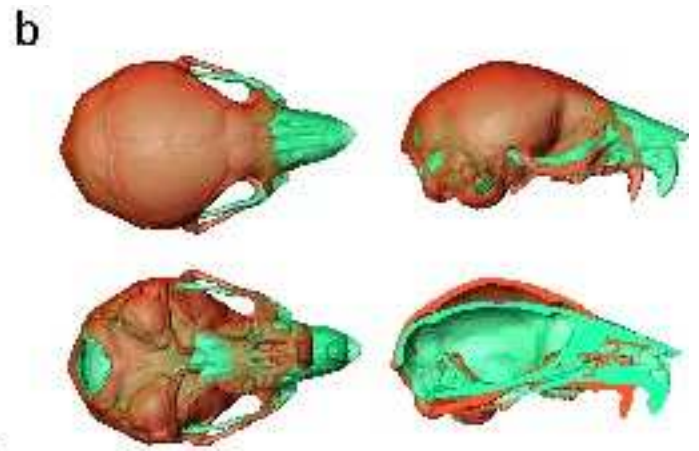
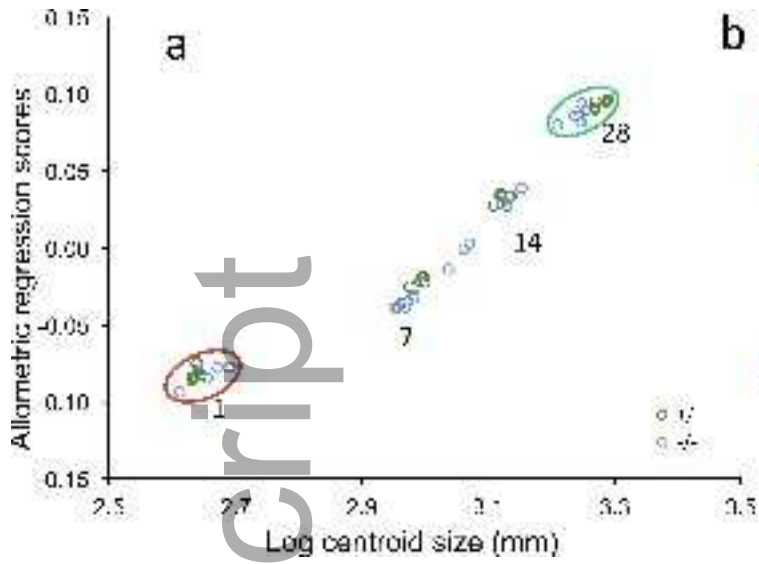


joa_13393_f1.tif

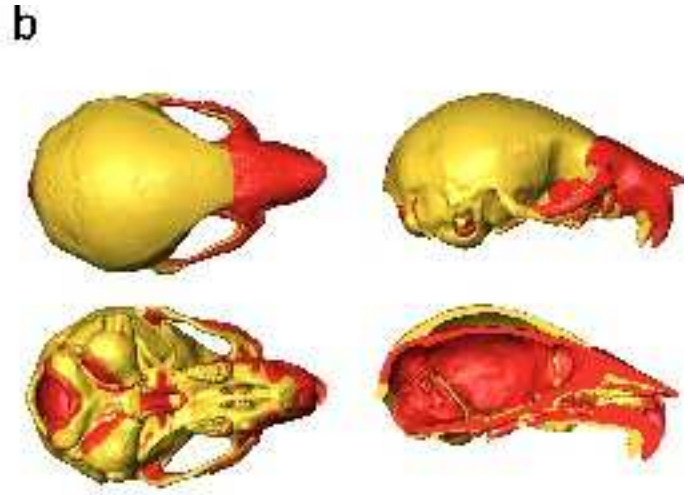
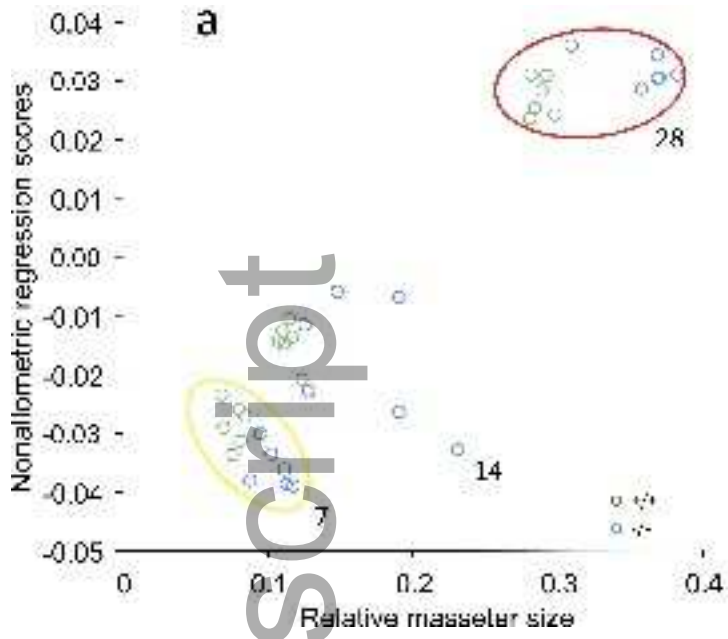




joa_13393_f3.tif

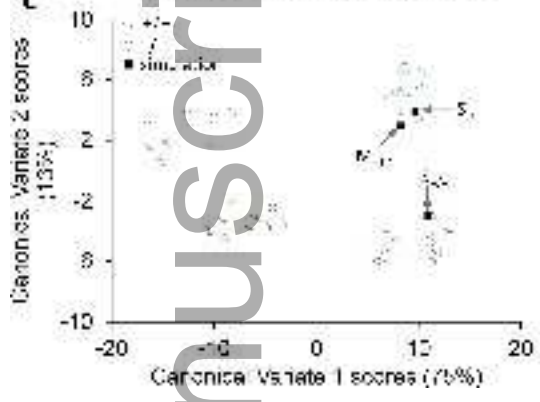
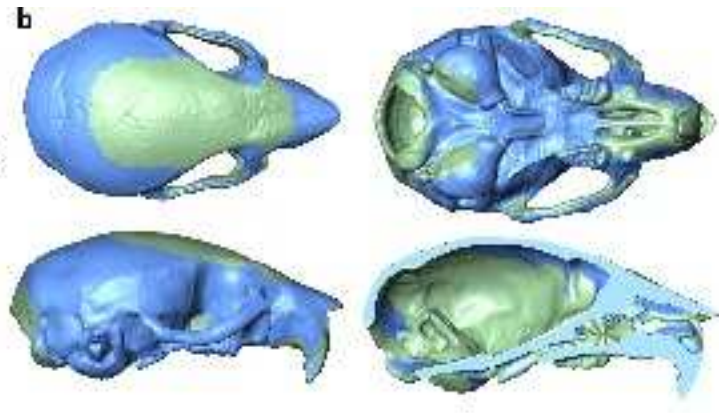
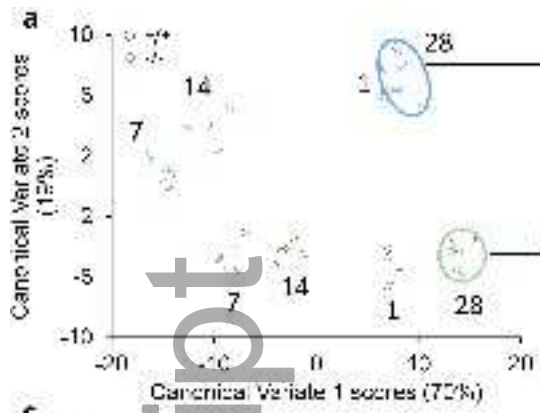


joa_13393_f4.tif



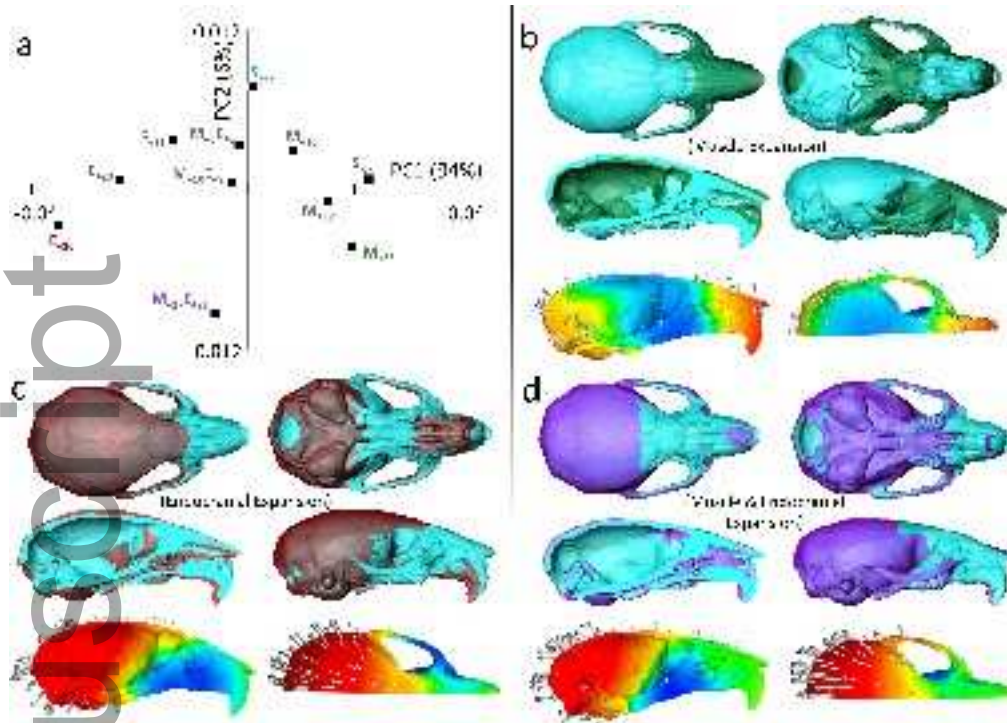
joa_13393_f5.tif

Author Manuscript

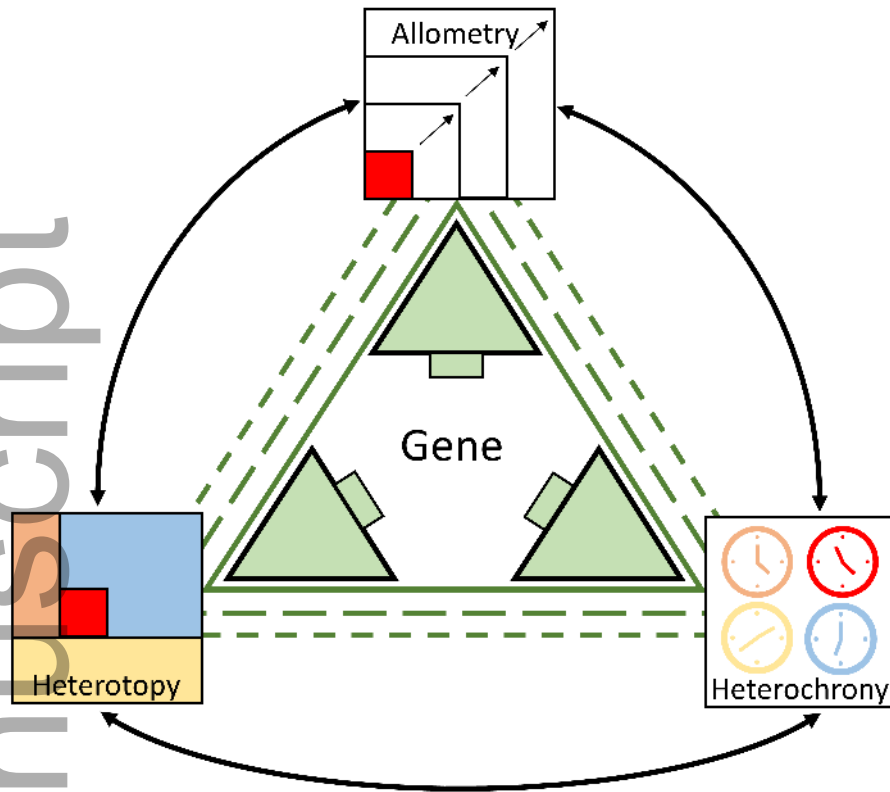


joa_13393_f6.tif

Author Manuscript



joa_13393_f7.tif



joa_13393_f8.tif